

1 **Earthquake Detectability and Depth Resolution with**  
2 **Dense Arrays in Long Beach, California: Further**  
3 **Evidence for Upper-Mantle Seismicity within a**  
4 **Continental Setting**

A. Inbal<sup>1</sup>, J.-P. Ampuero<sup>2</sup>, R. Clayton<sup>3</sup>

5 1. Department of Geophysics, Tel Aviv University, Tel Aviv, Israel

6 2. Université Côte d'Azur, IRD, CNRS, Observatoire de la Côte d'Azur, Géoazur, Valbonne,  
7 France

8 3. Seismological Laboratory, California Institute of Technology, Pasadena, CA, USA

**Declaration of Competing Interests**

9 The authors acknowledge there are no conflicts of interest recorded.

**Corresponding Author**

10 Asaf Inbal, Department of Geophysics, Tel Aviv University, Tel Aviv, Israel, Email: asafin-  
11 bal@tauex.tau.ac.il

**Abstract**

1 The Newport-Inglewood Fault (NIF) is a slowly-deforming fault cutting through a thin conti-  
2 nental crust with a normal geotherm, yet it hosts some of the deepest earthquakes in southern  
3 California. The nucleation of deep earthquakes in such a continental setting is not well under-  
4 stood. Moreover, the deep seismogenic zone implies the maximum NIF earthquake magnitude  
5 may be larger than expected. Here, we quantify the resolution of the Long-Beach (LB) and  
6 the Extended Long-Beach (ELB) dense arrays, used to study deep NIF seismicity. Previous  
7 study of the regional catalog and of downward-continued LB array data found NIF seismicity  
8 extending into the upper mantle beneath LB. Later studies, which analyzed the ELB raw data,  
9 found little evidence for such deep events. To resolve this inconsistency, we quantify the array's  
10 microearthquake detectability and resolution power via analysis of pre- and post-downward mi-  
11 grated LB seismograms, and benchmark tests. Downward migration focuses energy onto the  
12 source region and de-amplifies the surface noise, thus significantly improving detectability and  
13 resolution. The detectability is also improved with the increase in the array-aperture-to-source-  
14 depth ratio. The LB array maximum aperture is only 20% larger than the ELB aperture, yet  
15 its resolution for deep ( $>20$  km) events is improved by about a factor of two, suggesting that  
16 small changes to the array geometry may yield significant improvement to the resolution power.  
17 Assuming a constant aperture, we find the LB array maintain resolution with 1% of its sensors  
18 used for back-projection. However, the high sensor density is essential for improving the SNR.  
19 Analysis of the regional and array-derived NIF catalogs together with newly acquired Moho  
20 depths beneath the NIF, suggests mantle seismicity beneath LB is a robust feature of this fault.

## Introduction

21 Seismicity occurring within urban environments is difficult to characterize due to high levels of  
22 anthropogenic noise. For example, the Los Angeles (LA) basin, which is the densest population  
23 center in southern California, suffers from earthquake detectability that is far lower than the  
24 detectability in less-well instrumented regions. Dense array seismology, a methodology which  
25 utilizes finely sampled wavefields from closely-spaced seismometer- and smartphone-arrays [*Inbal*  
26 *et al.*, 2015, 2016, 2019; *Yang et al.*, 2021; *Yang and Clayton*, 2023] or fiber optic cables [*Zhan*,  
27 2020; *Lellouch et al.*, 2021], is well suited for signal detection in noisy environments. The main  
28 advantage of dense arrays over sparse networks is that dense wavefield sampling may be used  
29 suppress noise in data with poor signal-to-noise ratios (SNR). Furthermore, array back-projection  
30 may be used to focus incoming signals onto the source region, thereby strongly facilitating their  
31 location. However, it is not clear whether dense arrays, which are often deployed in noisy  
32 environments, and whose apertures do not exceed a few km, possess sufficient resolution power  
33 at seismogenic depths.

34 We restrict our analysis to geometries in which the potential source lies beneath the array, a  
35 situation common in dense array studies [e.g. *Inbal et al.*, 2015, 2016; *Peña Castro et al.*, 2019;  
36 *Catchings et al.*, 2020; *Yang et al.*, 2021, 2022; *Yang and Clayton*, 2023]. To investigate dense  
37 array source detectability and depth resolution, we consider the Long Beach (LB ; 5200 sensors ;  
38 deployed between January and June, 2011) and the Extended Long Beach (ELB ; 2500 sensors ;  
39 deployed between January and March, 2012) array datasets. The two arrays were located along  
40 adjacent portions of the Newport-Inglewood Fault (NIF), a major fault traversing the LA basin  
41 (Figure 1). *Inbal et al.* [2015, 2016, hereafter referred to as I2016 and I2015, respectively] used  
42 the LB dataset to compile a catalog for the portion of the NIF in LB, by enhancing the event

43 detectability via sub-array stacking and downward-continuation [*Gazdag, 1978*]. This allowed  
44 them to detect abundant seismicity occurring in the lower crust and upper mantle. The depth  
45 range was unusual given that, except for a few places, seismicity in southern California is generally  
46 confined to the upper 12 km or so [e.g. *Hauksson, 2011*]. Thus, I2016's findings challenged the  
47 common understanding regarding the physical mechanisms allowing faulting at depth. Recently,  
48 *Yang et al.* [2021, hereafter referred to as Y2021] introduced a new detection scheme which  
49 relies on the SNR of the back-projected surface data before and after trace randomization, and  
50 applied it to the ELB dataset. Given the proximity between the LB and ELB arrays, the similar  
51 deployment intervals, and lack of significant mainshocks during the deployment periods, the gross  
52 features of the LB and ELB seismicity catalogs must be quite similar. However, the discrepancy  
53 between I2015's and I2016's deep seismicity detection rates to Y2021's deep seismicity detection  
54 rates is very significant. Y2021 found that over a three month period 13 lower-crustal and 1 upper-  
55 mantle microearthquake had occurred below the ELB array. If we assume the deep seismicity  
56 rates below the LB and ELB arrays are similar, then I2016 and I2015 findings imply Y2021  
57 are missing 99% of the deep earthquakes below ELB. Y2021, on the other end, attribute the  
58 high detection rates in I2015's and I2016's catalogs to artifacts introduced in the back-projection  
59 procedure. Since the width of the NIF seismogenic zone determines the maximum magnitude the  
60 fault can produce, and since the physics governing the nucleation of upper-mantle earthquakes on  
61 continental transform faults is not well understood, it is important to resolve these discrepancies.  
62 Additionally, a growing number of studies rely on the detection of weak signals in back-projected  
63 seismic array data, underscoring the importance of quantifying the array resolution and the  
64 robustness of the detection scheme. In this study, we reexamine the NIF seismic catalogs along  
65 with newly acquired Moho depths in the LB area [*Clayton, 2020*]. We review the detection

66 schemes of I2015, I2016, and Y2021, and test what fraction of events detected by I2015 and  
67 I2016 might have been missed by Y2021. Then, we assess the discriminative power and depth  
68 resolution of dense arrays by using seismograms of deep NIF earthquakes and a set of synthetic  
69 tests. In light of these results, we confirm the findings of I2015 and I2016.

### Observing Deep Earthquakes on the LB array

70 To motivate the discussion on dense-array resolution, we begin by reviewing the available seis-  
71 micity catalogs and Moho depths, and the detections schemes of I2015, I2016, and Y2021. The  
72 distribution of seismicity along the NIF obtained from the LB array, and from the regional South-  
73 ern California Seismic Network (SCSN), together with newly acquired Moho depths [*Clayton,*  
74 2020] are shown in Figure 2. As was previously suggested by I2015 and I2016, many of the events  
75 in the LB section of the NIF occur in the lower crust, and some events occur in the upper mantle  
76 (Figure 2a). The frequency-magnitude distribution in the LB back-projection-based catalog is  
77 complete down to about  $M = -1$ . After adjusting for the area and time-window of the LB array  
78 deployment, the frequency-magnitude distribution of earthquakes occurring above 15 km depth  
79 in I2015 and I2016 catalogs nicely extrapolates to the frequency-magnitude distribution in the  
80 SCSN catalog, which is complete above  $M \sim 2$  [*Inbal et al., 2015*]. Note that the NIF intersects  
81 the Moho at about 17 km depth (Figure 2a). Thus, we think the LB array-derived catalog, which  
82 contains widespread lower-crustal seismicity observed over a 6-month period, but whose magni-  
83 tude of completeness is about three units lower than the SCSN catalog completeness magnitude,  
84 reflects the long-term behavior of the NIF and not some transient behavior. Additionally, note  
85 that both the SCSN and the LB array-derived catalog depths increase along the A-A' profile, and  
86 that this trend is consistent with the increase in Moho depth along the same profile. Accounting

87 for the combined uncertainty on the Moho and source depths suggests the deepest events in the  
88 SCSN catalog are well within the upper mantle.

89 An adjacent cross-section located below the ELB array is shown in Figure 2b. The focal depth  
90 distribution for the ELB section is skewed towards depth larger than 10 km, in disagreement  
91 with the distribution of Y2021, which mostly consists of events occurring in the upper 10 km  
92 (see Fig. 3 in Y2021). Given *Clayton* [2020]’s Moho depths, Y2021’s catalog contains 13 lower-  
93 crustal earthquakes and one or two upper-mantle earthquakes. Although the SCSN and QTM  
94 catalogs do not contain mantle earthquakes below ELB, the ELB focal depths are skewed towards  
95 values larger than the depth distribution observed along seismically active fault sections cutting  
96 through thin-crustal zones in southern California. Thus, similar to the LB section of the NIF,  
97 the regional catalogs suggest the ELB section also hosts earthquakes occurring at depths that  
98 are larger than the ones expected given the local geotherm and strain rates (see also discussion  
99 in I2016).

100 We find that the detection rate of earthquakes occurring at a depth between 12 and 20 km is  
101 somewhat lower in the QTM catalog than the in the SCSN catalog. This is likely due to the  
102 low number of available templates and the poor SNR conditions typical for the SCSN stations  
103 in the greater LA area. For example, a recent study found that a  $M \approx 1$  NIF and a  $M \approx 1$   
104 off-shore earthquake, showing  $\text{SNR} > 1$  on a number of stations located within 30 to 100 km from  
105 the epicenter, were missing from the SCSN and QTM catalogs [*Inbal et al.*, 2023]. Because the  
106 urban noise amplitude generally decays more rapidly with distance than the earthquake signal,  
107 the SNR of  $M \leq 1$  NIF events is sometimes higher on stations located outside the LA basin than  
108 on near-epicentral stations. This may cause traditional or template-based detection schemes to

miss some events, since those schemes rely primarily on phase arrivals observed on near-epicentral stations.

Unlike traditional network detection techniques, dense array analysis enhances the SNR by beamforming (i.e. delay-and-sum) the array's seismograms. Assuming the noise recorded by the array is uncorrelated between the array's sensors, this procedure improves the SNR by a factor proportional to  $\sqrt{N}$ , where  $N$  is the number of sensors in the array [e.g. *Rost and Thomas, 2002*]. If the target area lies beneath the array, and if a detailed velocity model is available, then further SNR improvement can be obtained by wavefield extrapolation using downward-continuation [*Gazdag, 1978*], which enhances near-vertical signals impinging on the array. We discuss the improvement in source-depth resolution due to downward-continuation in the section Spatial Resolution Analysis. Our experiments showed that strong LB surface noise sources were resilient to beamforming. Those sources showed as local maxima in the back-projected LB array images, making it difficult to discriminate between earthquake and noise signals. To improve the SNR of the LB data, I2015 and I2016 downward-continued them according to the following steps. I2015 and I2016 first stacked the array data over small sub-arrays, each of which consisting of 5 sensors, and then interpolated the sub-array-averaged data onto a regular grid. The interpolated data were Fourier transformed and then downward-continued to a depth of 5 km by applying a set of phase shifts whose magnitude was computed based on the local velocity model, frequency and wavenumber content (see I2015 and I2016 for further details). These steps significantly improved the SNR. Figure 3 illustrates the SNR improvement obtained by interpolating and downward-continuing an LB wavefield containing a signal from an earthquake which occurred 17 km beneath the array. The data were filtered between 2 and 8 Hz before they were downward continued. Visual inspection of these images discloses significant SNR

132 improvements leading to enhancements that facilitate the location procedure. Due to scattered  
133 strong noise sources, the amplitudes of the 2 to 8 Hz filtered surface data (Figure 3a) are not  
134 well-correlated with the epicentral location. Applying plain-stack (i.e. setting the inter-sub-array  
135 time-lags to zero) increases the amplitude of vertically propagating energy due to the deep source  
136 relative to horizontally propagating energy due to shallow sources, effectively suppressing isolated  
137 surface noise sources. The interpolation also removes some of the effects caused by isolated  
138 noise sources, each recorded by a few sensors (Figure 3b). Downward-continuation assumes the  
139 wavefield is composed only of vertically propagating energy, which is useful for removing surface  
140 waves, and for focusing vertical energy onto deep sources. These effects are clearly demonstrated  
141 in Figure 3c, which shows that most of the isolated surface noise-sources were de-focused, whereas  
142 energy from the deep earthquake is focused onto the source.

143 Following downward-continuation, I2015 and I2016 enveloped the data and back-projected  
144 them onto the volume beneath the LB array. The statistical attributes of the back-projected  
145 image maxima were analyzed. I2015 and I2016 found that the statistical distribution of the  
146 post-downward continued back-projection images containing newly identified tectonic sources  
147 was significantly different from the one associated with back-projection images of post-downward  
148 continued non-tectonic sources. The former follows a power-law distribution, while the latter  
149 follows a Gumbel distribution. That separation facilitated the discrimination stage. I2015 and  
150 I2016 declared a detection if the maximum amplitude of the back-projection image exceeded 5  
151 times the Median Absolute Deviation (MAD) of the amplitude of the back-projection images  
152 around the detection time. Using this detection threshold and the cumulative probabilities of  
153 the signal and noise back-projection images, I2015 found the false detection rate to be  $2 \times 10^{-3}$   
154 per night.

155 Y2021 took a different approach for discriminating coherent seismic sources from noise sources  
 156 in dense array recordings, which they refer to as Trace Randomization (TR). To test for the  
 157 presence of a tectonic signal, the TR scheme spatially redistributes envelopes of the array seis-  
 158 mograms by assigning them random positions within the array. The TR-detection criteria is  
 159 based on the degree of back-projected energy reduction due to the randomization, derived from  
 160 the ratio between the pre- and post-randomized maximal back-projected energy amplitudes as:

$$161 \quad R = 1 - \frac{E^{post}}{E^{pre}}, \quad (1)$$

162 where  $E^{pre}$  and  $E^{post}$  are the pre- and post-TR maximal energy levels, respectively. Neglecting  
 163 random uncorrelated noise fields which occasionally give rise to  $E^{post} > E^{pre}$ , Y2021 proposed an  
 164  $R$ -based detection criteria, applied to windows with  $E^{pre} > 5 \times MAD(E^{pre})$  around the detection  
 165 time. According to that scheme, uncorrelated noise sources should exhibit  $R \sim 0$ , while coherent  
 166 tectonic sources should exhibit  $R \sim 1$ . Thus, the statistical properties of a distribution of  
 167  $R$ -values computed over multiple time windows, would allow one to discriminate between deep,  
 168 temporally-isolated coherent sources to shallow uncorrelated noise sources common in continuous  
 169 urban dense array data.

170 Given that Y2021 found only a few deep NIF earthquakes, it is instructive to characterize  
 171 the LB and ELB array's capacity for detecting small-magnitude events in the pre-downward  
 172 continued data. We do that by employing the TR scheme on LB array data containing signals  
 173 from deep earthquakes occurring along the NIF. Many of the NIF earthquakes, which are located  
 174 directly beneath the LB and ELB arrays, exhibit poor surface SNR. Some of the events, however,  
 175 may be identified on the filtered pre-downward-continued array data. An example is shown in  
 176 Figure 4, which presents LB array data containing 5 earthquakes recorded during March 2011,  
 177 whose magnitudes were between 0 and 0.2, and whose focal depths were found to lie between

178 15 and 20 km. The top row shows the amplitudes of ground-velocity envelopes, computed by  
 179 filtering the seismograms between 2 and 10 Hz, squaring, and smoothing using a 0.1 s running  
 180 median window. The traces are ordered with respect to the hypocentral distance obtained by  
 181 I2016. For each trace we compute the P-wave train SNR by taking the ratio between the mean  
 182 energy in a 2 s window around the P-wave arrival to the mean in the 6 s preceding the event.  
 183 Panels a to e show the amplitudes for traces with  $\text{SNR} > 1$ , totaling about 40% of the array's  
 184 recordings. The seismic arrivals are clearly observed between 33 and 38 s in each of the record  
 185 sections (see also Figures S1-S5). The panels on the bottom row in Figure 4 show the distribution  
 186 of the SNR as a function of the sensor location. Note that in a few cases (e.g. panel f and i), the  
 187 epicenter is located near a cluster of high SNR traces. However, the surface detection pattern  
 188 is generally not well correlated with the epicentral location, which complicates the detection  
 189 procedure. For the earthquakes shown in Figure 4, the array-averaged SNR are between 1.02  
 190 and 1.06, within a few percent of the median SNR of LB events occurring below 15 km. Thus  
 191 these 5 events represent the SNR conditions of many of the deep earthquakes in the LB catalog.

192 We used the relation in Equation 1 to compute the  $R$ -values for the time windows containing  
 193 the arrivals in the seismograms shown in Figure 4a-e, and found that  $R$  varies between 0.01  
 194 and 0.2 for these five events. Y2021 state that time-windows they associated with noise had  
 195  $R > 0.2735$ , which is considered here as a threshold above which the Y2021 scheme would declare  
 196 a positive detection. Note that the  $R^{LB}$ -values calculated for the events in Figure 4 are lower  
 197 than the threshold of Y2021 for the ELB dataset. Note also, that because of its smaller aperture,  
 198 the  $R^{ELB}$  associated with arrivals as the ones shown in Figure 4 is expected to be smaller than  
 199  $R^{LB}$ . The strong presence of noise in the pre-downward continued ELB data and the conservative

200 detection criterion may explain why Y2021's scheme have missed many events below the ELB  
 201 array.

### Synthetic Tests for Characterizing the Effects of the Signal-to-Noise Ratio and Array Aperture on Source Discrimination

202 To examine why the LB back-projection energy reduction may sometime tend to 1 (i.e.  $R = 0$ )  
 203 for seismograms containing tectonic signals correlated among 40% of the array's sensors, and to  
 204 assess how the  $R$ -values are influenced by the array's aperture and SNR levels, we applied a series  
 205 of tests using two synthetic datasets. In the first set of tests, we generate synthetic seismograms  
 206 assuming a population of sources whose numbers exponentially decay with depth below 4 km,  
 207 similar to the source depth distribution in the LB catalog compiled by I2016. For each source,  
 208 we compute  $R^{ELB}$  and  $R^{LB}$  for a monochromatic 5-Hz input signal modulated by an envelope  
 209 whose amplitude decays exponentially with time over a time scale of a few seconds, and which  
 210 propagates in a uniform velocity model. The spectral content of the synthetic signal is selected  
 211 based on NIF earthquake seismograms analyzed by I2015 and I2016. We add white noise to  
 212 the seismograms such that their SNR is smaller than one, similar to urban dense-array datasets.  
 213 In the second set of tests, we compute  $R$  using traces containing uncorrelated random noise.  
 214 The results are presented in Figure 5. The blue curve in panel a shows the value of  $R^{ELB}$  as a  
 215 function of source depth. Note that  $R$ -values are depth-dependent, such that larger values are  
 216 systematically associated with sources at shallow depths, which implies that an  $R$ -based detector  
 217 may miss deep seismic events. This depth bias is only slightly reduced by increasing the aperture  
 218 of the array, as shown by the red curve in Figure 5a, which indicates  $R^{LB}$  values as a function  
 219 of source depth. Note that, since  $R^{LB} > R^{ELB}$ , the TR-based detection statistics obtained for  
 220 the ELB geometry by Y2021 do not apply straightforwardly to the LB array geometry. Also, the

value of  $R$  computed for the March 2011 earthquakes shown in Figure 4 is considerably smaller than the synthetic value, which likely reflects the poor SNR conditions (i.e. array-averaged SNR) of the LB array data. However, this does not affect the trend with depth shown in Figure 5a.

The results presented in Figure 5 provide further insights on the importance of the array aperture for source discrimination. That discrimination scheme is most effective for sources associated with a large scatter of the inter-array time delays, a requirement that is met when the array aperture is close to or larger than the source depth. When the aperture-to-source-depth ratio is large, TR is expected to significantly decrease  $E^{post}$  relative to  $E^{pre}$ , thereby providing a reliable detection statistic. For the LB and ELB arrays, this condition applies to events occurring above approximately 8 km and 12 km, respectively. On the other hand, when the aperture-to-source-depth ratio is much smaller than one, the range of inter-array time delays ("normal moveout") tends to zero, thereby reducing the discriminative power of the array. The discriminative power can be parametrized by the array's time-delay Median Absolute Deviation ( $MAD_{\Delta t}$ ), the value of which is dependent on the array aperture and source depth, as well as on the SNR and the time delay resolution. In general,  $MAD_{\Delta t}$  decreases with source depth, with faster decrease rates for small-aperture arrays (Figure 6). Thus, for very small arrays or very deep sources, we expect  $MAD_{\Delta t} \rightarrow 0$ . The narrow range of time-delays obtained in these situations is expected to yield  $R$ -values close to zero, and therefore cause the detector to miss some weak events.

The array's discriminative power is also affected by the SNR. For poor-SNR signals, the ratio  $E^{post}/E^{pre}$  can occasionally be significantly smaller than one, which may result in a false detection. To illustrate this effect, we indicate in Figure 5 the  $R^{ELB}$ -value reported by Y2021, and the one obtained in this study by the dashed and yellow vertical lines, respectively. Note that

244 Y2021's  $R^{ELB}$ -value was computed using thousands of time windows passing their initial detec-  
245 tion criteria, whereas the  $R^{ELB}$  reported here is a depth-averaged value computed using only  
246 windows containing a coherent synthetic source, yet the two values closely match. Since most of  
247 the windows Y2021 used for computing  $R^{ELB}$  likely do not contain a tectonic signal, this result  
248 suggests the  $R$ -based scheme may not be suitable for discriminating deep sources. We find this  
249 issue repeats when the approach is applied to data containing random uncorrelated noise. For  
250 this type of input, the fluctuations around the mean value of  $R$  can be quite large, and are gener-  
251 ally dependent on factors such as the sampling interval and the envelope calculation method. For  
252 the commonly used  $n$ th-root stacking [e.g. *Rost and Thomas, 2002*, with  $n=3$ ], the average value  
253 of  $R$  is close to 0, as expected for records containing only uncorrelated random noise. However,  
254 after neglecting cases in which  $R < 0$ , we find that 34% the windows have  $0 < R < 0.3$  and 13%  
255 of the windows have  $0.3 < R < 0.6$  (see dark and light-grey rectangles in panel 5a), within the  
256 range of results from tests containing a coherent source (blue curve in Figure 5a). In fact, the  
257 range of depths allowing for reliable source discrimination on the pre-downward migrated ELB  
258 array is limited to the upper 8 km, since the statistics for deeper sources are not significantly  
259 different from the ones associated with a random noise field.

260 Thus far, we have estimated the detection sensitivity to the array aperture and SNR. Next, we  
261 estimate the source depth error by comparing the source depth obtained from back-projecting  
262 the LB signal envelopes to the input source depth, after adding white uncorrelated noise. The  
263 noise amplitude is uniformly distributed over the range between -0.8 and 0.8 times the maximum  
264 envelope amplitude. The results are presented in Figure 5b,c, which shows the distribution of  
265 source depth discrepancies and the depth error as a function of input LB source depth. We find  
266 that the source depth error is about 2 km, consistent with the results of synthetic tests presented

267 by I2016. In addition, for the range of source-aperture-to-source-depth ratios examined here,  
268 we do not find that the depth error correlates with the source depth. This suggests that the  
269 dominant factor limiting accurate source depth determination is the array aperture, assuming  
270 the sources lie within the array’s footprint, and that their signals exceed the noise level. Thus,  
271 resolving the depth of earthquakes occurring beneath the array may be obtained by a subset of  
272 the array’s sensors, given that (1) the source-depth-to-array-aperture ratio is smaller than about  
273 2, and (2) the SNR is larger than 1. We test the validity of this statement by using synthetic  
274 tests presented in the next section.

### Spatial Resolution Analysis

275 The results presented in the previous section show that the  $R$ -based detector is likely to miss  
276 low-SNR signals excited by deep tectonic sources. Because of its smaller aperture, the number of  
277 events missed by the ELB array is expected to be larger than the number missed by the LB array.  
278 Once a signal has been positively detected, however, its location accuracy is dependent on the  
279 SNR and array geometry. Given the LB SNR levels, its vertical location resolution is about 2 km  
280 (Figure 5b). To characterize the source imaging resolution, we use Point Spread Functions (PSF),  
281 which describe the effect of the imaging system on the imaged object [e.g. *Lecomte et al.*, 2015;  
282 *Nakahara and Haney*, 2015]. The degree of source resolution and illumination may be derived  
283 from basic principles of ray theory, by considering the density of source-to-array raypaths. In  
284 this framework, a well illuminated source is defined as one for which ray paths cover a large  
285 fraction of the focal sphere. In an isotropic medium, the wavenumber vector is at any point  
286 perpendicular to the wavefront, and thus its orientation and amplitude in the source region may  
287 be used to determine the source image spatial resolution. For a source at location  $j$  imaged by  
288 a station at location  $i$ , the local wavenumber vector is defined by the projection of the source

289 Fourier components onto the local slowness vector [*Lecomte et al.*, 2015]:

$$290 \quad k_{ij}^{local} = \omega \cdot S_{ij}, \quad (2)$$

291 where  $\omega$  represents the angular frequency, and  $S_{ij}$  is the local slowness vector, which is parallel to  
 292 the ray connecting the  $j$ 'th source with the  $i$ 'th station. In practice, each frequency component  
 293 is weighted by the source spectra, and as a result, wideband sources are expected to be better  
 294 resolved than narrowband sources. The spatial resolution is also dependent on the aperture of the  
 295 array. Increasing the array aperture will increase the local wavenumber density, which improves  
 296 the illumination and enhances the imaging resolution. The PSF is obtained from  $k^{local}$  after  
 297 weighting by the source spectra by summing over available source-to-array ray paths, and then  
 298 taking the inverse spatial Fourier transform. The advantage of this approach is that it allows  
 299 us to compute PSFs that are independent of the noise, and ensures that the spatial variability  
 300 of urban noise levels [*Riahi and Gerstoft*, 2015; *Inbal et al.*, 2019] does not affect the resolution  
 301 estimates.

302 To quantify the spatial resolution and analyze its dependency on the source depth, we compute  
 303 the PSF for the LB and ELB array geometries. As input, we use the spectra of the envelope  
 304 of the 5 Hz exponentially decaying sine function discussed in the previous section. Equation  
 305 2 is solved assuming a uniform velocity model of 3.5 km/s, neglecting the effects of scattering  
 306 on the PSF [*Lecomte et al.*, 2015]. Figure 7 presents the spatial resolution for shallow (10 km;  
 307 panels a,b) and deep (20 km; panels c,d) sources. In the absence of noise in the input data and  
 308 velocity model, the only effect reducing the source depth resolution is the limited aperture of  
 309 the array, which is manifested by the smearing of the PSFs along the depth axis. This affects  
 310 the ELB and LB array differently, and is most noticeable for sources located below 12 km, for  
 311 which the vertical resolution of the ELB degrades rapidly with depth. To illustrate this effect,

we present in Figure 7e the vertical resolution scale, defined as the vertical extent over which the PSF value decreases down to 80% relative to the maximum PSF value at the focal point. For shallow sources ( $< 10$  km), both arrays can well resolve sources located less than 1 km apart. However, the limited aperture of the ELB array yields images whose resolution power at large depths is reduced relative to the LB array. Events located at depths larger than about 20 km are not well resolved by the ELB array, but may be resolved by the LB array. This effect is an outcome of a modestly wider aperture (both in the NS and in the EW direction ; see Figure 1) of the LB array relative to the ELB array.

We also investigated the effects of downward-continuation [Gazdag, 1978] of the wavefield on the vertical resolution. Reducing the vertical separation by wavefield extrapolation has the desired effect of increasing the  $MAD_{\Delta t}$ . The direct consequence is a significant increase in the vertical resolution scale. This is illustrated by the dashed curve in Figure 7e, showing the vertical resolution for the LB array after wavefield extrapolation down to 5 km depth. For the deepest events located below 25 km, downward continuation may improve the vertical resolution by as much as 40%. Note that these estimates provide a lower bound on the improvement in the resolution. The SNR may be improved prior to conducting downward continuation by applying plain-stack (i.e. setting the array's time delays equal to zero) of small sub-arrays within the LB array, which tends to de-amplify surface waves generated by shallow sources Figure (3a). Additionally, downward continuation further de-amplifies such arrivals (Figure 3b), and is thus expected to improve the vertical resolution relative to what is shown in Figure 7e.

Recent studies suggest the dramatic increase in the spatial sampling of the seismic wavefield provided by state-of-the-art seismic imaging systems may help improve earthquake detectability and hence refine existing catalogs [Inbal et al., 2019; Lellouch et al., 2021; Mesimeri et al.,

335 2021; *Arrowsmith et al.*, 2022]. For example, *Inbal et al.* [2019] evaluated the earthquake location  
336 accuracy achieved by dense noisy smartphone arrays. They found that back-projecting only 0.5%  
337 of the available smartphone-derived seismograms in the LA area would allow detection of events  
338 with  $M \sim 1$ , approximately one magnitude unit below the catalog magnitude of completeness  
339 in that region. This smartphone-user density was required in order to enhance the SNR of  
340 smartphone-recorded signals due to  $M \sim 1$  earthquakes. However, it is not clear what is the  
341 minimum density required in order to resolve the location of back-projected signals that stand out  
342 of the noise level.

343 Next, we use a bootstrap analysis to assess the sensitivity of location estimates of signals with  
344  $\text{SNR} > 1$  to the density of the array. To do that, we compute the PSF for the LB configuration  
345 by using only 1% of the available LB sensor positions, which we refer to as the sparse array  
346 configuration. For each input source depth value, we generate 100 sparse configurations randomly  
347 selected from the LB array sensor locations. The results are presented in Figure 7e, which  
348 shows the average resolution of the vertical location of the source for the sparse array dataset.  
349 Remarkably, we find that the sparse configuration is almost as effective as the dense configuration  
350 for resolving earthquake-like signals with  $\text{SNR} > 1$  located beneath the array. Moreover, we find  
351 that the resolution on deep ( $> 15$  km) sources obtained by using the sparse configuration exceeds  
352 the resolution of the 2500-sensors ELB array for sources lying at this depth range. Thus, an array  
353 whose dimensions are comparable to the LB array, but which contains only a small number of  
354 sensors, can be used to locate signals excited by deep tectonic events if they exceed the ambient  
355 noise level, and occur within the array's footprint. The logic also applies to the local seismic  
356 network operating in the LA area, whose inter-sensor distances are of the order of 10 km. Back-

357 projecting signals recorded by this network onto the NIF fault may help obtain robust locations,  
358 and reduce the local catalog’s magnitude of completeness [Inbal *et al.*, 2023].

## Summary

359 We examine the depth resolution of dense seismic arrays for sources lying beneath the array. We  
360 find that the parameter controlling the resolution power is the source-depth-to-array-aperture  
361 ratio and the source’s bandwidth. The source-array geometry effect on the resolution can be  
362 parameterized by the MAD of the inter-array time delay distribution, which is sensitive to modest  
363 changes in the aperture. The LB array maximum aperture is only 20% larger than the ELB array  
364 maximum aperture, yet its source depth resolution for deep ( $>20$  km) events is improved by about  
365 a factor of two (Figure 5), which indicates that small changes to the array geometry may yield  
366 significant improvement to the resolution power. In addition, we find that using only 1% of the  
367 LB array sensors does not significantly affect the depth resolution of signals with  $\text{SNR} > 1$ , given  
368 the sensor subset maintains an aperture close to aperture of the entire array.

369 We use synthetic tests to evaluate the performance of the TR -based approach of Y2021. We  
370 find that this scheme is sensitive to the array aperture, and is expected to detect more shallow-  
371 depth events than deep events. This sensitivity also suggests the results obtained by Y2021 for  
372 the ELB dataset may not straightforwardly apply to the LB dataset. In addition, the TR-based  
373 scheme may sometimes classify a random noise field as a tectonic signal. This is demonstrated  
374 in the following manner: if we assume the input source depths are exponentially distributed and  
375 truncated below 35 km, and that all time windows contain arrivals from no more than a single  
376 earthquake, then we find the mean  $R^{ELB}$ -value equal to 0.278 (dashed curve in panel 5b). This  
377 value is almost identical the  $R^{ELB}$  value computed by Y2021 for noise-dominated time windows.

378 The factors promoting earthquake nucleation below the seismogenic zone remain poorly re-  
379 solved. Earthquakes are the result of stick-slip frictional instabilities that occur due to brittle  
380 fracture of rock, a behavior that is strongly dependent on the ambient pressure-temperature,  
381 lithology, strain rate, and pore pressure. In southern California, the maximum depth of seis-  
382 micity largely coincides with the 400°C isotherm [*Bonner et al.*, 2003; *Hauksson*, 2011]. That  
383 correlation is thought to manifest thermal effects on the rheology, with the deep termination of  
384 seismicity corresponding to the onset of plastic yielding in Quartz-rich rocks [e.g. *Scholz*, 2002].  
385 Clusters of deep events are common in thick-crustal, rapidly-deforming regions, where the local  
386 isotherm is depressed downwards due to lower-than-average heat-flow [*Bonner et al.*, 2003], or  
387 where faults cut through mafic lithology [*Magistrale and Sanders*, 1996; *Magistrale*, 2002], which  
388 tend to exhibit brittle behavior at larger depths. The NIF events are an exception to this rule.  
389 They represent some of the deepest earthquakes in California, yet they occur on slowly deforming  
390 faults cutting through the thinnest crust in California, whose associated heat flow is close to the  
391 regional average. Thus, the width of the seismogenic zone along the NIF challenges our under-  
392 standing of the processes responsible for earthquake rupture. Since the maximum earthquake  
393 magnitude for a given fault is a function of its width, the seismicity depth extent also bears  
394 strong implications for seismic hazard in the LA urban area.

395 **Data and Resources.** The Southern California Earthquake Data Center earthquake catalog  
396 is available at the following doi: <https://scedc.caltech.edu>. The LB seismicity catalog is from  
397 *Inbal et al.* [2016], and the ELB seismicity catalog is from *Yang et al.* [2021]. The raw LB data  
398 are protected by a license agreement with Signal Hill Petroleum, and will be provided by the  
399 authors upon request.

**Acknowledgments.** We thank three anonymous reviewers for constructive remarks that greatly improved the quality of this manuscript. This research was supported by ISF grant #1802/22.

## References

- Arrowsmith, S. J., D. T. Trugman, J. MacCarthy, K. J. Bergen, D. Lumley, and M. B. Magnani (2022), Big Data Seismology, *Rev. Geophys.*, *60*(2), e2021RG000,769, doi: <https://doi.org/10.1029/2021RG000769>.
- Bonner, J. L., D. D. Blackwell, and E. T. Herrin (2003), Thermal Constraints on Earthquake Depths in California, *Bull. Seis. Soc. Am.*, *93*(6), 2333–2354, doi:10.1785/0120030041.
- Catchings, R. D., M. R. Goldman, J. H. Steidl, J. H. Chan, A. A. Allam, C. J. Criley, Z. Ma, D. S. Langermann, G. J. Huddleston, A. T. McEvelly, D. D. Mongovin, E. M. Berg, and Y. Ben-Zion (2020), Nodal Seismograph Recordings of the 2019 Ridgecrest Earthquake Sequence, *Seismo. Res. Lett.*, *91*(6), 3622–3633, doi:10.1785/0220200203.
- Clayton, R. W. (2020), A detailed image of the continent-borderland transition beneath Long Beach, California, *Geophys. J. Int.*, *222*(3), 2102–2107, doi:10.1093/gji/ggaa286.
- Gazdag, J. (1978), Wave equation migration with the phase-shift method, *Geophysics*, *13*(7).
- Hauksson, E. (2011), Crustal geophysics and seismicity in southern California, *Geophys. J. Int.*, *186*(1), 82–98, doi:10.1111/j.1365-246X.2011.05042.x.
- Inbal, A., R. W. Clayton, and J.-P. Ampuero (2015), Imaging widespread seismicity at mid-lower crustal depths beneath Long Beach, CA, with a dense seismic array: Evidence for a depth-dependent earthquake size distribution, *Geophys. Res. Lett.*, *42*(15), 6314–6323, doi:10.1002/2015GL064942.

- 421 Inbal, A., J.-P. Ampuero, and R. W. Clayton (2016), Localized seismic deformation in  
422 the upper mantle revealed by dense seismic arrays., *Science*, *354*(6308), 88–92, doi:  
423 10.1126/science.aaf1370.
- 424 Inbal, A., Q. Kong, W. Savran, and R. M. Allen (2019), On the Feasibility of Using  
425 the Dense MyShake Smartphone Array for Earthquake Location, *Seismo. Res. Lett.*, doi:  
426 10.1785/0220180349.
- 427 Inbal, A., T. Cristea-platon, J.-p. Ampuero, G. Hillers, and D. Agnew (2023), Reply to “Comment  
428 on ‘Sources of Long-Range Anthropogenic Noise in Southern California and Implications for  
429 Tectonic Tremor Detection’ by Asaf Inbal, Tudor Cristea-Platon, Jean-Paul Ampuero, Gregor  
430 Hillers, Duncan Agnew, and Susan E. Hough” by Allie Hutchison, Yijian Zhou, and Abhijit  
431 Ghosh, *Bull. Seismo. Soc. Am.*, pp. 1–15, doi:10.1785/0120200007.
- 432 Lecomte, I., P. Lubrano-Lavadera, A. Wuestefeld, T. Kaschwich, J. Albaric, and H. N. Gharti  
433 (2015), Focusing in migration-based location of weak microseismicity: modelling point-spread  
434 function for resolution analyses, in *SEG Technical Program Expanded Abstracts 2015*, pp. 2491–  
435 2495, Society of Exploration Geophysicists, doi:10.1190/segam2015-5813282.1.
- 436 Lellouch, A., R. Schultz, N. Lindsey, B. Biondi, and W. Ellsworth (2021), Low-  
437 Magnitude Seismicity With a Downhole Distributed Acoustic Sensing Array—Examples  
438 From the FORGE Geothermal Experiment, *J. Geophys. Res.*, *126*(1), e2020JB020,462, doi:  
439 10.1029/2020JB020462.
- 440 Magistrale, H. (2002), Relative contributions of crustal temperature and composition to control-  
441 ling the depth of earthquakes in Southern California, *Geophys. Res. Lett.*, *29*(10), 87–1–87–4,  
442 doi:10.1029/2001GL014375.

- 443 Magistrale, H., and C. Sanders (1996), Evidence from precise earthquake hypocenters for segmen-  
444 tation of the San Andreas Fault in San Geronio Pass, *J. Geophys. Res.*, *101*(B2), 3031–3044,  
445 doi:10.1029/95JB03447.
- 446 Mesimeri, M., K. L. Pankow, and J. Rutledge (2021), A Frequency-Domain-Based Algorithm  
447 for Detecting Microseismicity Using Dense Surface Seismic Arrays, *Bull. Seismo. Soc. Am.*,  
448 *111*(5), 2814–2824, doi:10.1785/0120210062.
- 449 Nakahara, H., and M. M. Haney (2015), Point spread functions for earthquake source imag-  
450 ing: an interpretation based on seismic interferometry, *Geophys. J. Int.*, *202*(1), 54–61, doi:  
451 10.1093/gji/ggv109.
- 452 Peña Castro, A. F., S. L. Dougherty, R. M. Harrington, and E. S. Cochran (2019), Delayed  
453 Dynamic Triggering of Disposal-Induced Earthquakes Observed by a Dense Array in Northern  
454 Oklahoma, *J. Geophys. Res.*, *124*(4), 3766–3781, doi:10.1029/2018JB017150.
- 455 Riahi, N., and P. Gerstoft (2015), The seismic traffic footprint: Tracking trains, aircraft, and  
456 cars seismically, *Geophys. Res. Lett.*, *42*(8), 2674–2681, doi:10.1002/2015GL063558.
- 457 Ross, Z. E., D. T. Trugman, E. Hauksson, and P. M. Shearer (2019), Searching for hidden earth-  
458 quakes in Southern California., *Science*, *364*(6442), 767–771, doi:10.1126/science.aaw6888.
- 459 Rost, S., and C. Thomas (2002), Array seismology: Methods and applications, *Reviews of Geo-*  
460 *physics*, *40*(3), 1008, doi:10.1029/2000RG000100.
- 461 Scholz, C. (2002), *The Mechanics of Earthquakes and Faulting*, Cambridge University Press.
- 462 Yang, L., X. Liu, and G. C. Beroza (2021), Revisiting evidence for widespread seismicity in the  
463 upper mantle under Los Angeles., *Science Adv.*, *7*(4), eabf2862, doi:10.1126/sciadv.abf2862.
- 464 Yang, L., X. Liu, W. Zhu, L. Zhao, and G. C. Beroza (2022), Toward improved urban earthquake  
465 monitoring through deep-learning-based noise suppression, *Science Adv.*, *8*(15), eabl3564, doi:

466 10.1126/sciadv.abl3564.

467 Yang, Y., and R. W. Clayton (2023), Shallow Seismicity in the Long Beach–Seal Beach, California  
468 Area, *Seismo. Res. Lett.*, *94*(4), 1948–1956, doi:10.1785/0220220358.

469 Zhan, Z. (2020), Distributed Acoustic Sensing Turns Fiber-Optic Cables into Sensitive Seismic  
470 Antennas, *Seismo. Res. Lett.*, *91*(1), 1–15, doi:10.1785/0220190112.

## Addresses

471 • Asaf Inbal , asafinbal@tauex.tau.ac.il, Department of Geophysics, Tel Aviv University, P.O.  
472 Box 39040, Tel Aviv 6997801, Israel

473 • Jean-Paul Ampuero , ampuero@geoazur.unice.fr, Université Côte d’Azur, IRD, CNRS, Ob-  
474 servatoire de la Côte d’Azur, Géoazur, boulevard de l’Observatoire CS 34229 06304 Nice cedex  
475 04, France

476 • Robert Clayton, clay@gps.caltech.edu, California Institute of Technology, Seismological Lab-  
477 oratory, 1200 E. California Blvd., MS 252-21 Pasadena, California 91125-2100

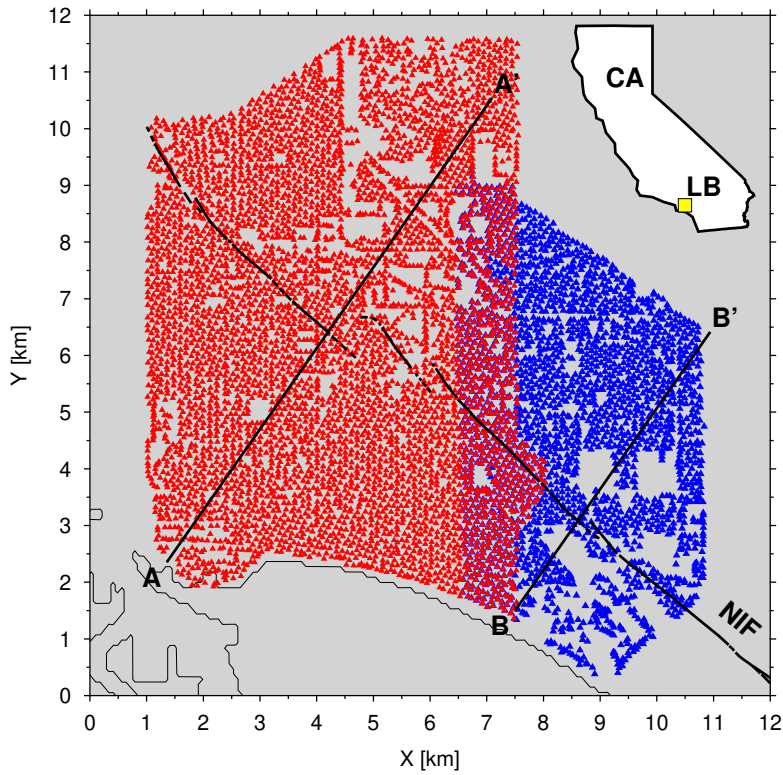


**Figure 1.** Location map. Red and blue triangles indicate the locations of the LB and ELB array sensors, respectively. The thick black line shows the location of the Newport-Inglewood Fault. Lines A-A' and B-B' refer to depth cross-sections shown in Figure 2. Thin black line marks the coastline. Inset map shows the location of Long Beach within the state of California. Abbreviations: NIF: Newport-Inglewood Fault, LB: Long Beach, CA: California.

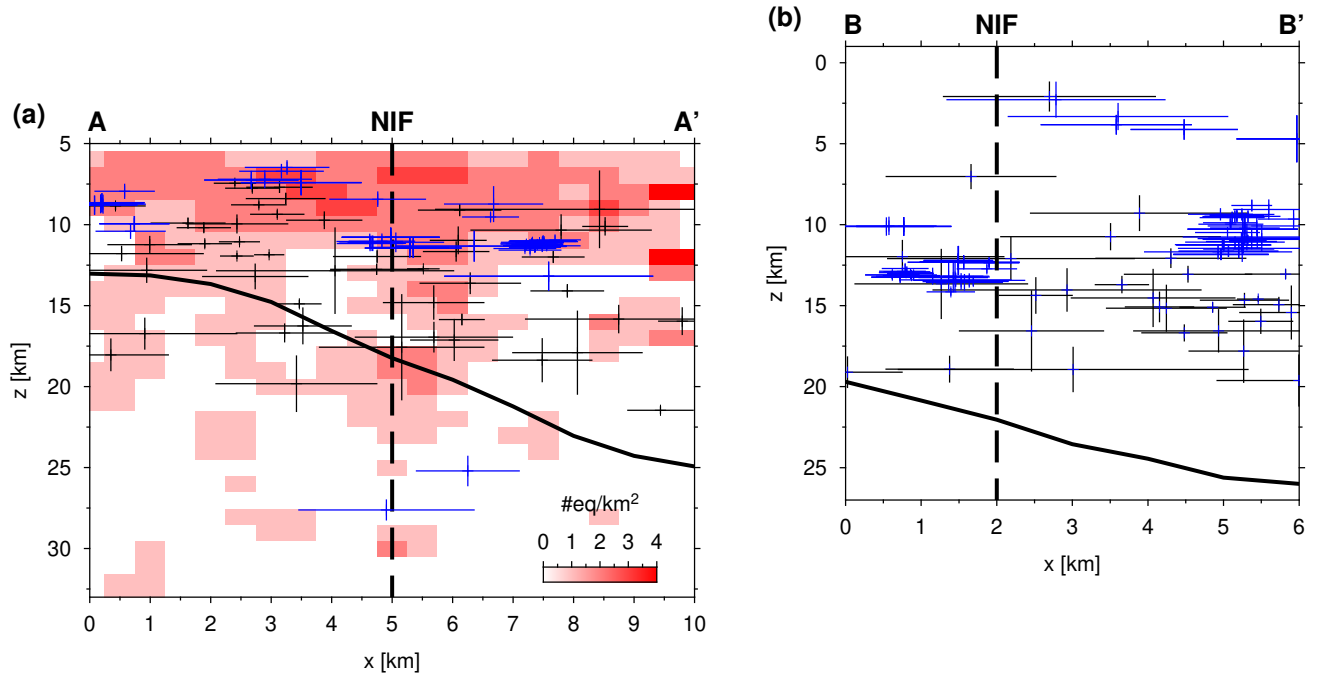


**Figure 2.** LB seismicity and Moho depth cross-sections. Earthquake densities from the LB array [Inbal *et al.*, 2016] are shown in shades of red. Black and blue crosses indicate the locations of earthquakes found in the regional Southern California Earthquake Center seismicity catalog covering the period between 2005 and 2024, and in the match-filter-based catalog of Ross *et al.* [2019] (QTM) covering the period between 2008 and 2018, respectively. Size of crosses corresponds to the location uncertainty. Solid and dashed curves are for the Moho depth [Clayton, 2020], and the Newport-Inglewood Fault, respectively. Red stars in panel b are for the locations in Yang *et al.* [2021]’s ELB catalog. The location of the cross-sections are shown in Figure 1. a. LB cross-section. b. ELB cross-section.

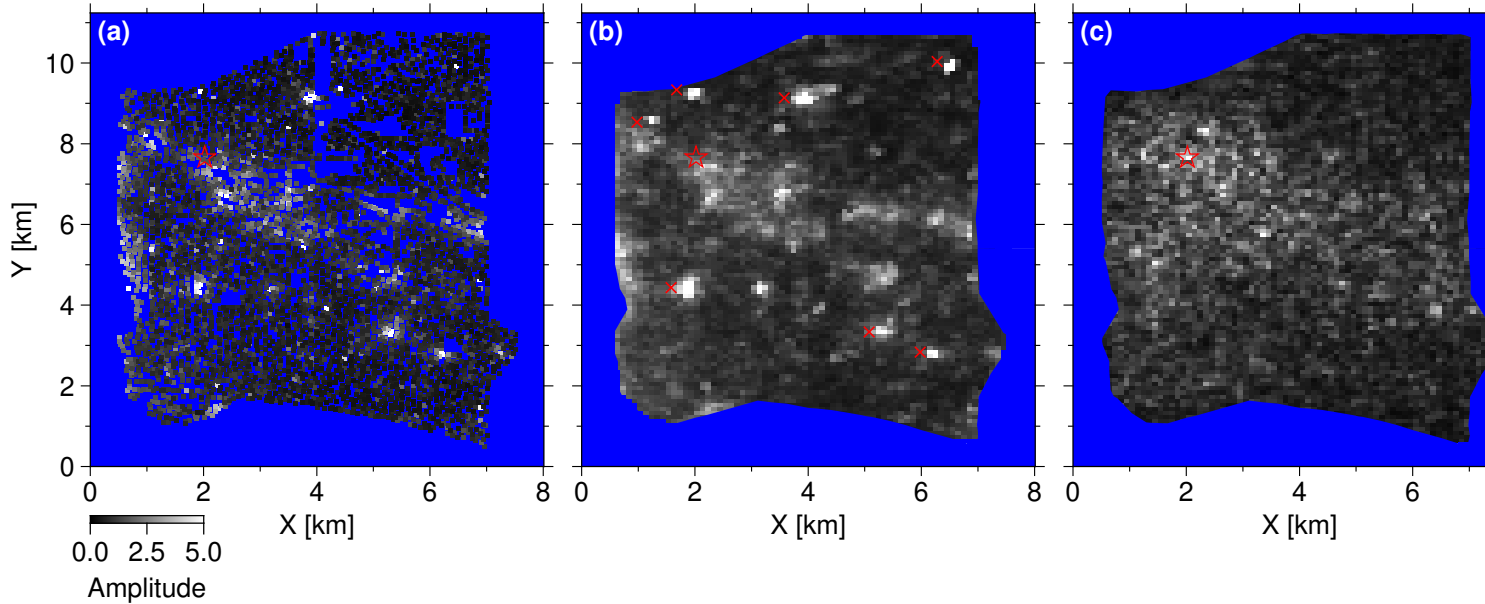


**Figure 3.** Example of interpolation and downward-continuation of the LB array data. Input data are the LB array amplitudes for the  $M0.1$  of March 16, 2011. Event depth was determined by I2016 to be 17 km (see Figure 4a,f). Amplitudes are normalized with respect to the mean array amplitude in each panel. Star indicates the epicentral location. Crosses in panel b highlight strong surface noise sources whose amplitude was decreased by de-focusing during the downward continuation stage. (a) LB array data filtered between 2 and 8 Hz. (b) LB array data after sub-array stacking and interpolation. (c) LB array data after downward continuation to a depth of 5 km.

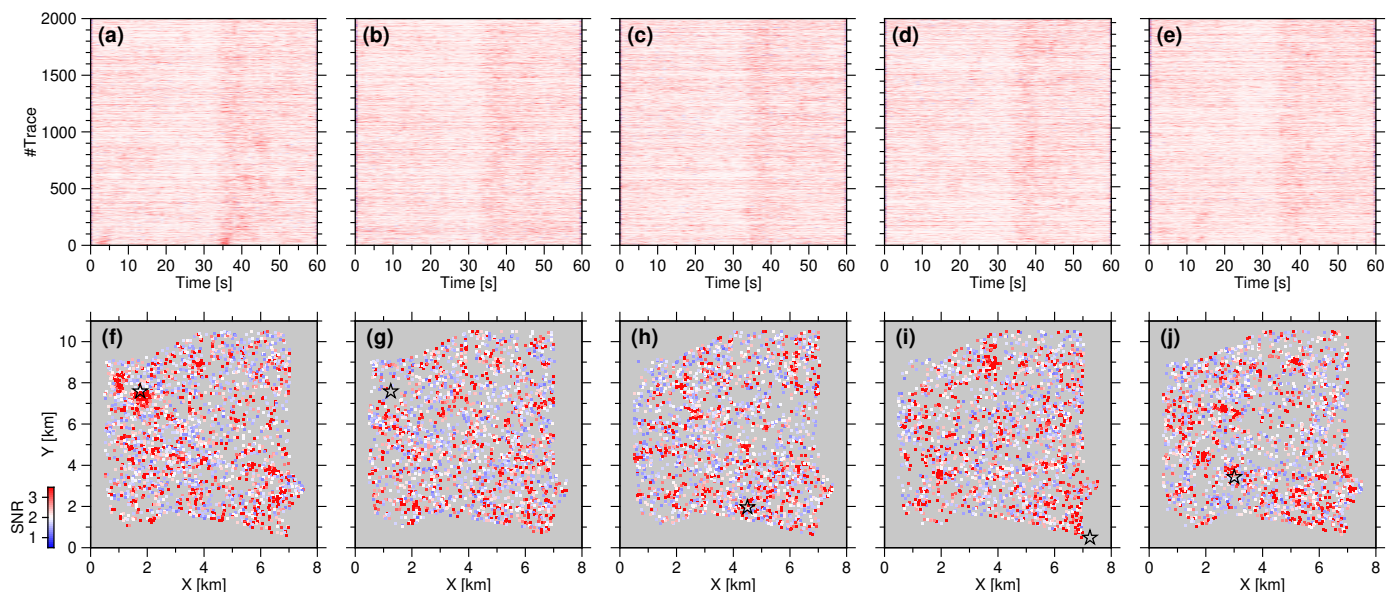


**Figure 4.** Seismograms recording arrivals from earthquakes occurring during March 2011 beneath the LB array. Top row shows the 2 to 10 Hz envelope amplitudes as a function of time for 2000 traces with  $\text{SNR} > 1$ . Bottom row shows the distribution of the maximal amplitudes relative to the pre-event noise as a function of location. The star indicates the epicentral location. Day of detection, magnitude and depth are as follows: a,f March 16, 2011,  $M0.1$ , 17 km ; b,g March 18, 2011,  $M0.1$ , 17 km ; c,h March 8, 2011,  $M0.06$ , 16 km ; d,i March 15, 2011,  $M0.2$ , 16 km ; e,j March 5, 2011,  $M0.07$ , 19 km.

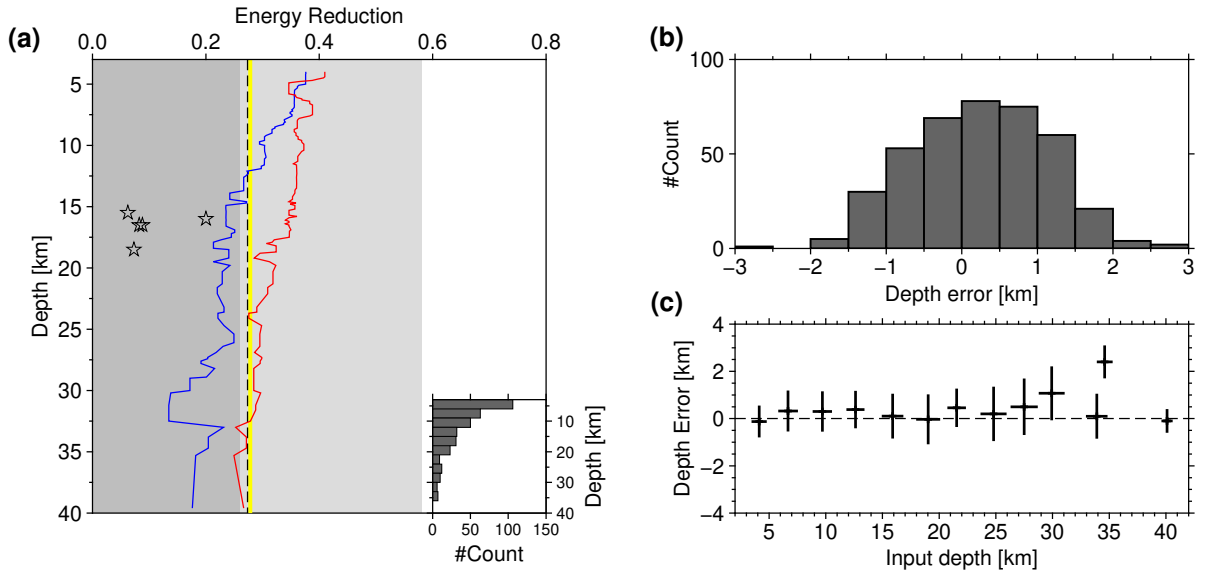


**Figure 5.** Synthetic tests for source discrimination using Trace Randomization. a. The back-projected energy reduction as a function of the input source depth. Solid lines indicate the level of energy reduction (defined in Equation 1), for synthetic tests in which the input source depths are exponentially distributed (as in the inset histogram), with blue and red colors for the ELB and LB array, respectively. Dashed vertical line indicates the mean back-projected energy reduction for the ELB data reported by *Yang et al., 2021*, and the yellow line indicates the depth-averaged back-projected energy reduction we obtain for the ELB array. Dark and light grey rectangles indicate the 1- and 2-sigma intervals around the mean stack energy reduction for noise-only input using the ELB array geometry. Stars indicate the energy reduction computed for the 5 NIF earthquakes shown in Figure 4. b. The distribution of source depth error for the LB array. c. The LB source depth error as a function of the source input depth.

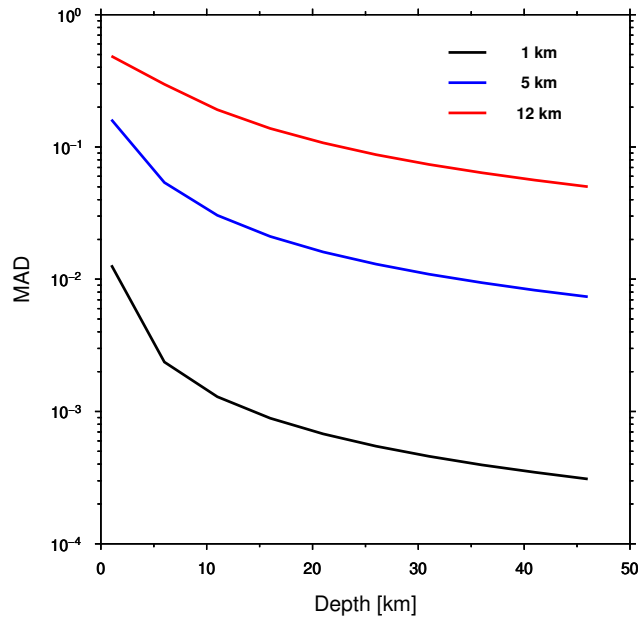


**Figure 6.** The median absolute deviation of the inter-array time delays as a function of the source depth. Black, blue, and red curves are for 1, 5, and 12 km array apertures, respectively. Travel times are calculated assuming a uniform velocity equal to 3.5 km/s.

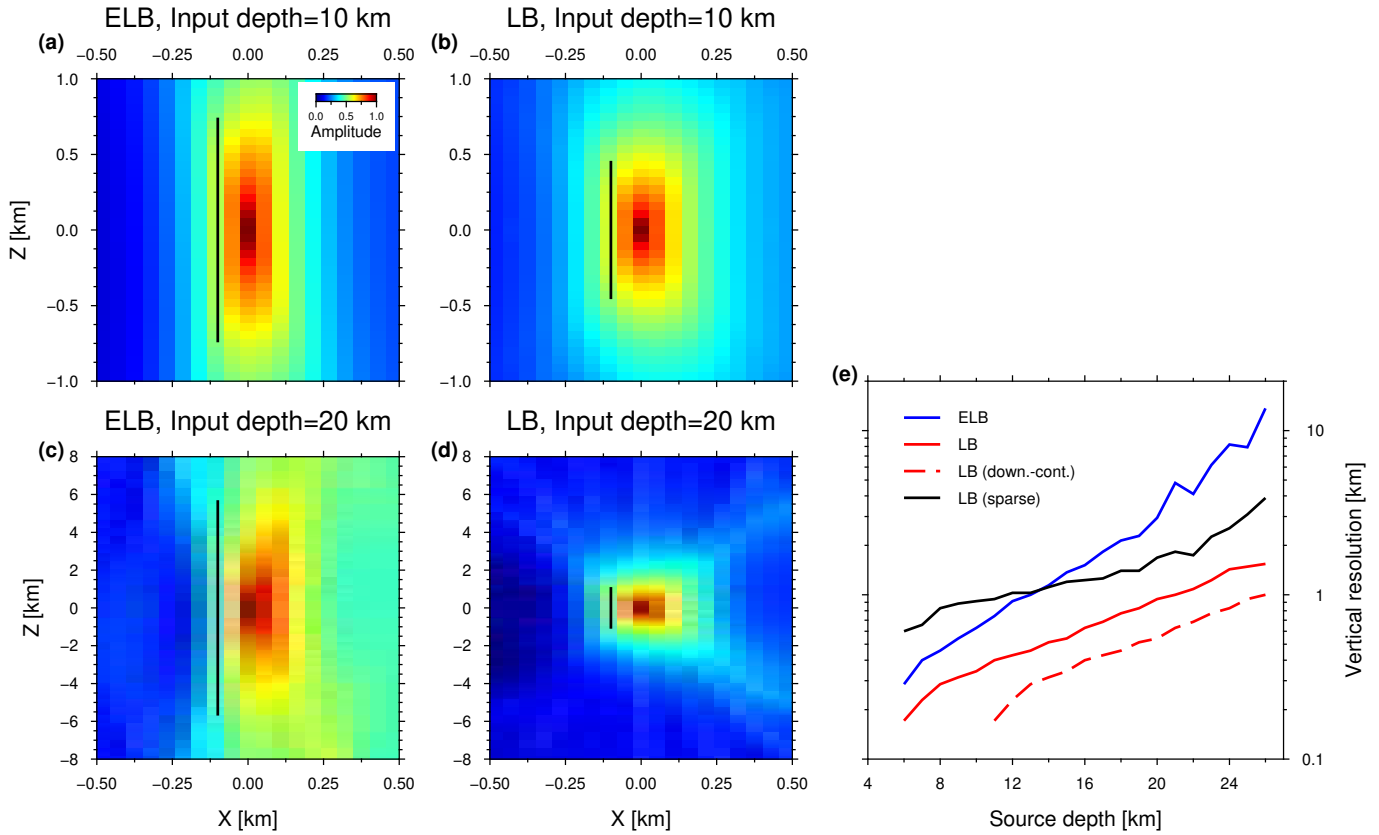


**Figure 7.** Resolution analysis. a-d. Point spread functions computed for an input source located at depth of 10 km (panels a,b) and 20 km (panels c,d). Vertical lines indicate the vertical resolution, defined as the length scale over which the resolution power decreases down to 80% of the maximum. a,c. ELB array. b,d. LB array. e. The vertical resolution scale as a function of source depth. Blue and red solid curves are for the ELB and LB array, respectively. Dashed red curve indicates the LB array vertical resolution after downward continuation. Black solid curve indicates the vertical resolution obtained using 1% of the LB array sensors.